Chromium clustering and ordering in $Hg_{1-x}Cr_xSr_2CuO_{4+\delta}$

O. Chmaissem, D. N. Argyriou, D. G. Hinks, and J. D. Jorgensen
Materials Science Division and Science and Technology Center for Superconductivity, Argonne National Laboratory, Argonne, Illinois 60439

B. G. Storey, H. Zhang, L. D. Marks, Y. Y. Wang, and V. P. Dravid
Department of Materials Science and Engineering and Science and Technology Center for Superconductivity, Northwestern University, Evanston, Illinois 60208

B. Dabrowski
Physics Department, Northern Illinois University, DeKalb, Illinois 60115
(Received 6 July 1995)

Solid-solution compounds where Cr, Re, and other metals are substituted for Hg in Hg-Ca-Ba-Cu-O superconductors have been reported to exhibit enhanced flux-pinning behavior. We have determined the structural modifications resulting from the incorporation of Cr in $Hg_{1-x}Cr_xSr_2CuO_{4+\delta}$ (for $x \approx 0.4$) using neutron powder diffraction, electron diffraction, and lattice imaging. Cr substitutes at the Hg site, but is displaced to allow tetrahedral coordination by oxygen atoms. Additional oxygen is incorporated to provide four oxygen atom neighbors for each Cr atom. These CrO_4 units cluster to form a supercell of approximate dimensions $5a \times 5a \times 2c$ in which Cr-rich and Hg-rich regions alternate in all three crystallographic directions. Because the Cu-O apical bond associated with the CrO_4 unit is lengthened to 3.13 Å, the superconducting planes are best viewed as consisting of CuO_5 pyramids, oriented up or down as dictated by the supercell ordering, rather than CuO_6 octahedra. Local structural constraints associated with individual Cr sites require that considerable disorder is present, even in the supercell. Extended defects in this supercell (e.g., columns of CuO_6 octahedra associated with Hg-rich regions) may contribute to the enhanced flux pinning.

INTRODUCTION

A remarkable enhancement of flux-pinning behavior achieved by chemical substitution in $HgBa_2Ca_{n-1}Cu_nO_{2n+2+\delta}$ compounds has recently been reported by Shimoyama *et al.*[1,2] In earlier experiments it had been found that substitution of Cr (and later Re) on the Hg site enabled the synthesis of $(Hg,Cr)Sr_2CuO_{4+\delta}$, where all of the Ba had been replaced by the smaller Sr ion.[3] These new Sr-substituted compounds were initially of interest because of their improved chemical stability. It was later realized that these new materials exhibited flux-pinning properties substantially better than the Ba-containing compounds.[1] This behavior was attributed to the decrease in the interlayer distance, i.e., the thickness of the blocking layer between CuO_2 planes, resulting from the smaller Sr ions. Decreasing this distance would be expected to increase flux pinning by increasing the coupling between pancakelike vortices to form vortex lines.[4,5]

In later work, however, Shimoyama *et al.* used high-pressure synthesis techniques to partially substitute Cr, Mo, or Re on the Hg site without the replacement of Ba by Sr.[2] These compounds also showed enhanced flux pinning, even though the interlayer distance was not shortened (and, in fact, was lengthened slightly in some cases). Thus it was concluded that shortening of the interlayer distance could not be solely responsible for the enhanced flux pinning.

Prior to these reports, such enhancements of flux-pinning behavior were achieved only by methods such as radiation damage.[6–11] The ability to enhance flux pinning by chemical substitution provides opportunities for the study of the structure modifications that can give rise to such phenomena and, more importantly, could lead to the development of processing methods that will be applicable on an industrial scale and will have substantial impact on the utilization of these materials.

In this paper we report the structure of the solid-solution compound $Hg_{1-x}Cr_xSr_2CuO_{4+\delta}$ (for $x \approx 0.4$) as determined by neutron powder diffraction, electron diffraction, and lattice imaging. The local structures around Cr and Hg atoms are sufficiently different that a refinement of the average structure projected into the fundamental tetragonal unit cell provides a clear picture of the distortions resulting from the incorporation of Cr. Electron diffraction and lattice imaging show how Cr- and Hg-rich regions order in all three crystallographic directions to form a supercell of approximate dimensions $5a \times 5a \times 2c$. Cr is incorporated in the form of CrO_4 tetrahedra, resulting in a dramatic lengthening of the corresponding Cu-O apical bond to 3.13 Å. Thus the CuO_6 octahedra of the ideal $HgBa_2CuO_{4+\delta}$ structure are, in effect, replaced by CuO_5 pyramids that point either up or down as dictated by the supercell ordering. Because the dimensions of the alternating Cr- and Hg-rich regions are smaller than typical magnetic vortex dimensions and they are ordered into a regular lattice, the supercell structure is not likely to explain the enhanced flux pinning. However, local constraints that govern how individual CrO_4 tetrahedra can arrange themselves into clusters require that considerable disorder must exist in the supercell. Evidence for this disorder is seen in the electron-diffraction data. Extended defects in the supercell,

0163-1829/95/52(21)/15636(8)/$06.00

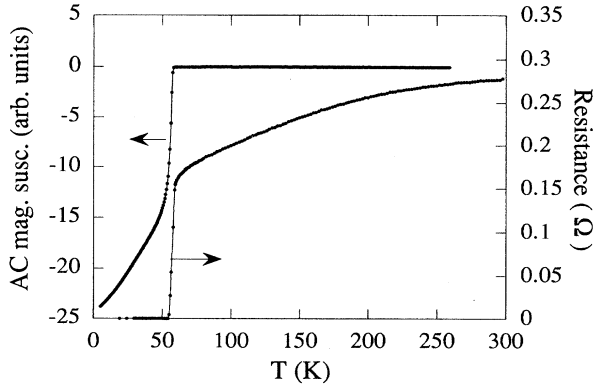

FIG. 1. Resistivity and ac magnetic susceptibility measurements for $(Hg_{1-x}Cr_x)Sr_2CuO_{4+\delta}$ showing a sharp superconducting transition around 60 K.

for example, extended Hg-rich regions resulting in columns of CuO_6 octahedra, could explain the enhanced flux pinning.

SYNTHESIS AND CHARACTERIZATION

For the study of the solid-solution structure, we synthesized a sample with a large Cr concentration. HgO, Cr_2O_3, $Sr(NO_3)_2$, and CuO powders were mixed to provide an overall composition of $Hg_{0.7}Cr_{0.3}Sr_2CuO_{4+\delta}$. First, a $Cr_xSr_2CuO_z$ precursor was prepared by reacting the mixed powder at 700 °C for 3 h and then at 900 °C for 18 h in flowing oxygen gas. Then HgO was added to the precursor and the sample was pelletized and sealed in an evacuated quartz tube which was heated at a rate of 3.5 °C/min to 870 °C. The sample was maintained at this temperature for 6 h before cooling at a rate of 3.5 °C/min to room temperature. The resulting sample showed $(Hg,Cr)Sr_2CuO_{4+\delta}$ as the major phase and $SrCuO_2$ and $SrHgO_2$ as impurity phases, resulting in a Cr concentration higher than that of the starting composition. The superconducting properties were studied by ac magnetic susceptibility and resistivity measurements, as shown in Fig. 1. The superconducting transition temperature was about 60 K.

NEUTRON POWDER DIFFRACTION

Neutron-powder-diffraction measurements were performed on the Special Environment Powder Diffractometer at Argonne's Intense Pulsed Neutron Source.[12] Data were analyzed by the Rietveld technique, using the GSAS code,[13] over the d-spacing range 0.5–4 Å, which included 1289 Bragg peaks. Since no supercell reflections were visible in the neutron-diffraction data, the average structure (i.e., superposition of cells containing either Cr or Hg) was refined, with partial occupancies for the sites associated with Cr and Hg local environments. This technique provides useful information in the present case because the local structures in the vicinity of Cr and Hg are sufficiently different to be resolved using the neutron-powder-diffraction data. $SrCuO_2$ and $SrHgO_2$, which appear in small concentrations, were included as impurity phases in the Rietveld refinement. Figure 2 shows the raw diffraction data and best-fit Rietveld profile. Refined values of the widths of diffraction lines were comparable to the instrument resolution, suggesting no significant strain or particle size broadening.

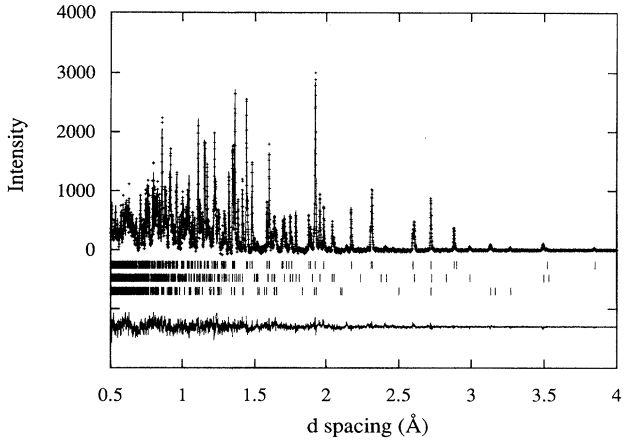

FIG. 2. Best-fit Rietveld refinement profile showing observed (+) and calculated (line) data. The markers below the profile correspond to Bragg peak positions for (top to bottom) $(Hg_{1-x}Cr_x)Sr_2CuO_{4+\delta}$, $SrHgO_2$, and $SrCuO_2$. The difference between observed and calculated values is shown at the bottom. The refined background has been subtracted.

It was found that Cr substitutes for Hg (as expected), but the Cr atoms are displaced from the ideal (0,0,0) site along the ⟨100⟩ direction. This displacement allows the Cr atom to achieve a tetrahedral coordination to four oxygen-atom neighbors. Two of these neighbors are the original apical oxygen atoms [O(2)] which are displaced to a new $(x,0,z)$ site, O(2)′, to form the appropriate bonds to Cr. Interstitial oxygen [O(3)] provides the other two oxygen atoms for the

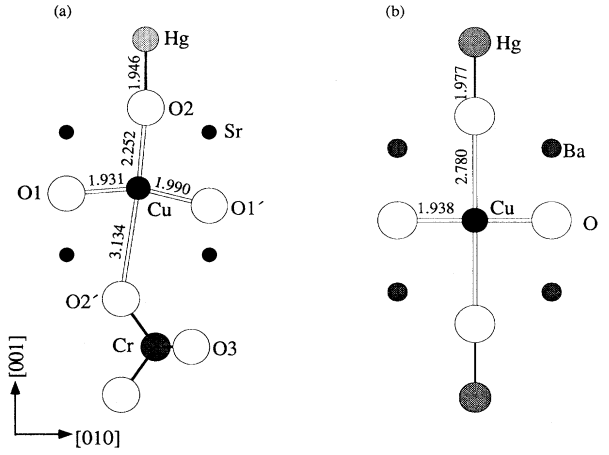

FIG. 3. (a) Proposed local structure for $Hg_{1-x}Cr_xSr_2CuO_{4+\delta}$ based on refinement of an average structure model of the fundamental cell dimensions using neutron-powder-diffraction data. Cr atoms achieve tetrahedral coordination by displacing the apical oxygen atoms to a new site [O(2)′] and incorporating two additional oxygen atoms per Cr atom at the in-plane site O(3). The coordinated tilting of CuO_6 octahedra and spatial constraints on the placement of O(3) atoms tends to produce the local Cr ordering shown. Bond lengths are in Å units. (b) The ideal structure of $HgBa_2CuO_{4+\delta}$ (Ref. 14) is shown, for comparison.

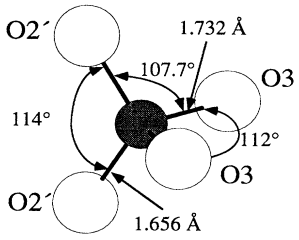

FIG. 4. Bond lengths and angles between Cr and its surrounding oxygen atoms. A near perfect tetrahedron is formed.

tetrahedron around Cr. These O(3) oxygen atoms are also displaced from the ideal interstitial (1/2,1/2,0) site, along the ⟨110⟩ direction to an $(x,x,0)$ site (with $x \approx 0.372$) to achieve appropriate bond lengths to Cr. Each Cr atom pulls enough interstitial oxygen [O(3)] into the structure to achieve tetrahedral coordination to oxygen. The fraction of displaced apical oxygen atoms, $n[O(2)']$, is nominally equal to the number of interstitial oxygen atoms, $n[O(3)]$. One might expect $n[O(3)] > n[O(2)']$ since additional interstitial oxygen may be required to create carriers in the CuO_2 planes. Such a difference is observed, but our error bars are not small enough to assign any physical significance to this observation. The local structure around the Cr site is illustrated in Fig. 3.

In modeling a structure such as this, in which atoms are displaced from their ideal (high-symmetry) sites, multiple new sites are produced. In the actual structure, only one of these sites can be occupied, since the multiple sites are typically too close together to allow simultaneous occupation. Thus the actual local structure violates the symmetry of the average structure being used as a refinement model. We have selected a combination of Cr, O(2)′, and O(3) sites that defines a nearly perfect CrO_4 tetrahedron, as shown in Fig. 4. This configuration together with the short Cr-O bond lengths suggests that Cr is in the +6 state.

In addition to the displacements of near-neighbor oxygen atoms around the Cr site, we observe a significant displacement along the c-axis of part of the oxygen atoms in the CuO_2 plane. In the final refinements, part of the planar oxygen was placed at the ideal (1/2,0,1/2) site, O(1), and part was placed at a (1/2,0,z) site, O(1)′. The Cu atoms were also found to be displaced out of the plane. The best refinement model was found to be one in which all Cu atoms were displaced along z by a small amount. These displacements in the CuO_2 plane can be readily understood in terms of the asymmetry of the environment above and below the CuO_2 plane. We learned from electron diffraction (discussed later) that the Cr atoms order such that Cr and Hg atoms alternate along the c axis. Thus, for Cr concentrations approaching 50%, each Cu atom has a Cr atom below and an Hg atom above, as illustrated in Fig. 3, or vice versa. Some planar oxygen atoms have a similar asymmetric environment, with two Cr atoms above and two Hg atoms below (or vice versa), while other planar oxygen atoms have one Cr and one Hg, both above and below, yielding no asymmetry along z. Thus, assuming a Cr concentration near 50%, we have displaced all of the Cu sites, but only part of the planar oxygen sites. The choice of this model was also supported by R-value-ratio tests. These displacements of Cu and planar oxygen atoms are consistent with our proposal for the ordering that gives rise to the supercell structure, which will be discussed later. The final structural model and the refined parameters are given in Table I.

In order to test the uniqueness of the refinement model, alternate models that allow atom displacements along different directions were compared. For the analysis of these data, a number of alternate models were evaluated. It was found, for example, that displacements of Cr along the ⟨100⟩ direction gave better fits than displacements along the ⟨110⟩ direction. Likewise, displacements of the apical oxygen atom [ideal site O(2)] to an $(x,0,z)$ position gave better fits than to an (x,x,z) position. Split or displaced sites for Cu and O(1) were found to give significantly better fits than allowing anisotropic temperature factors for these atoms. Larger than normal temperature factors for the Hg, O(2), and Sr atoms indicate that these atoms are also displaced from their ideal sites. These displacements are to be expected. However, the magnitudes are within the resolution of our data (typically

TABLE I. Refined structural parameters for $(Hg_{1-x}Cr_x)Sr_2CuO_{4+\delta}$. Tetragonal structure of space group $P4/mmm$ and lattice parameters $a = 3.850\,00(7)$ Å, and $c = 8.6961(2)$ Å, $R_p = 3.05\%$, $R_{wp} = 4.67\%$, $\chi^2 = 1.758$. Constraints: $n(Hg)+n(Cr)=1$; $n[O(1)]+n[O(1)']=2$; $n[O(2)]+n[O(2)']=2$; $U[O(1)]=U[O(1)']$.

Atom	Position	x	y	z	U (Å^2)	n
Hg	1a	0	0	0	U_{11}: 0.029(3)	0.50(1)
					U_{22}: 0.029(3)	
					U_{33}: 0.009(2)	
Cr	4l	0.119(7)	0	0	0.002(5)	0.50(1)
Sr	2h	1/2	1/2	0.3017(2)	0.0168(6)	2
Cu	2g	0	0	0.5172(5)	0.0020(7)	1
O(1)	2e	1/2	0	1/2	0.0020(6)	1.26(6)
O(1)′	4i	1/2	0	0.5408(2)	0.0020(6)	0.74(6)
O(2)	2g	0	0	0.2237(12)	U_{11}: 0.029(2)	1.33(6)
					U_{22}: 0.029(2)	
					U_{33}: 0.016(4)	
O(2)′	8s	0.113(4)	0	0.160(3)	0.010(4)	0.67(6)
O(3)	4j	0.628(1)	0.628(1)	0	0.026(3)	0.88(3)

TABLE II. Selected bond lengths (Å) for $Hg_{1-x}Cr_xSr_2CuO_{4+\delta}$ compared to those of $HgBa_2CuO_{4+\delta}$.

	$HgBa_2CuO_{4+\delta}$ (Ref. 14)	$Hg_{1-x}Cr_xSr_2CuO_{4+\delta}$
Cu-O(1)	1.9375(1)	1.9308(3)
Cu-O(2)	2.780(1)	2.252(11)
Cu-O(1)′		1.990(5)
Cu-O(2)′		3.134(25)
Ba(Sr)-O(1)	2.7284(9)	2.584(1)
Ba(Sr)-O(2)	2.8716(5)	2.805(2)
Ba(Sr)-O(3)	2.836(1)	2.715(2)
Sr-O(1)′		2.834(14)/2.362(11)
Sr-O(2)′		2.726(8)/3.28(2)
Hg-O(2)	1.977(1)	1.946(10)
Hg-O(3)	2.7401(1)	2.810(1)
Cr-O(2)′		1.656(22)
Cr-O(3)		1.732(16)
CrO_4 tetrahedron angles		
O(2)′-Cr-O(3)		107.7(2)°
O(2)′-Cr-O(2)′		114(2)°
O(3)-Cr-O(3)		112(2)°

less than 0.2 Å). For this reason, we chose not to assign displaced sites to these atoms. For Hg and O(2), the refined anisotropic temperature factors indicate that the maximum displacements are in the plane, as expected.

Bond lengths and angles for the $Hg_{1-x}Cr_xSr_2CuO_{4+\delta}$ structure are compared to those for the ideal $HgBa_2CuO_{4+\delta}$ structure[14] in Table II (see also Fig. 3). The c axis (which, for a single-Cu-layer compound, is the "blocking layer" distance) is shortened by 8.6%, from 9.5132 to 8.6961 Å. This results from the substitution of the smaller Sr ion at the Ba site and the smaller dimensions of the CrO_4 unit along the c axis. One apical oxygen atom, O(2)′, is strongly bonded into the CrO_4 unit, resulting in a very long Cu-O(2)′ apical bond, 3.13 Å. As a result of this and in response to the overall shortening along the c axis, the other apical bond, Cu-O(2), is shortened substantially to 2.25 Å. Cu-O apical bonds this short (2.29 Å) are present in $YBa_2Cu_3O_{7-\delta}$,[15] but are quite unusual for copper-oxide superconductors. However, a very similar arrangement occurs in $(Cu,C)Ba_2Ca_3Cu_4O_{11+\delta}$ where the blocking layer consists of a random arrangement of copper-oxygen chains and CO_3 units.[16] The apical oxygen atoms associated with the CO_3 units are bonded to the Cu atoms at a distance of 3.18 Å, while those associated with the copper-oxygen chains are bonded at a distance of 2.39 Å. The asymmetry around the Cu site, with a Hg atom above and a Cr atom below (or vice versa), results in the displacement of the Cu atom off its ideal site towards Hg. The resulting CuO_6 octahedron is so asymmetric that it is probably better viewed as a pyramid rather than an octahedron, since the O(2)′ is so far away from Cu. Even though the a-axis length is slightly shorter (3.850 vs 3.875 Å), one of the in-plane copper-oxygen bond lengths [Cu-O(1)′] is longer than in the ideal structure, as a result of the significant buckling of the plane. Bond lengths involving Hg, O(2), or Sr atoms are subject to some additional uncertainty since small displacements of these atoms are indicated by their larger than normal temperature factors.

ELECTRON DIFFRACTION AND MICROSCOPY

Although the neutron-powder-diffraction data are analyzed in terms of the basic $HgBa_2CuO_{4+\delta}$ tetragonal unit cell, electron-diffraction measurements done on the same samples show that the actual structure is a supercell of approximate dimensions $5a\times5a\times2c$. The supercell reflections are clearly defined in the electron-diffraction data and were always found in the diffraction patterns along the right zones (for instance, ⟨110⟩, ⟨111⟩, etc). Hundreds of grains have been checked. No other superlattices were found. Even though these superlattice spots are not visible in the neutron-powder-diffraction data (much lower sensitivity compared to that of the electron beam), a fairly detailed picture of the actual structure emerges by combining the electron-diffraction results with what is learned about the local structure from neutron diffraction.

Transmission electron microscope (TEM) samples were prepared by crushing powder from the neutron-diffraction sample in two drops of anhydrous methanol and dispersing it onto clean 1000-mesh TEM grids. These grids were immediately inserted into the microscope to limit contamination. High-resolution electron microscope (HREM) images and electron-diffraction patterns were taken using a Hitachi H9000 and a Philips CM30 operated at 100 and 300 kV. Negatives were digitized to 8 bits using an Optronics P1000 densitometer and analyzed with Semper 6 software. Northwestern University multislice imaging software (NUMIS) was used to simulate electron-diffraction patterns and HREM images.

Electron-diffraction patterns for the major zone axes ⟨001⟩, ⟨100⟩, and ⟨110⟩ are shown in Figs. 5(a)–5(c). All

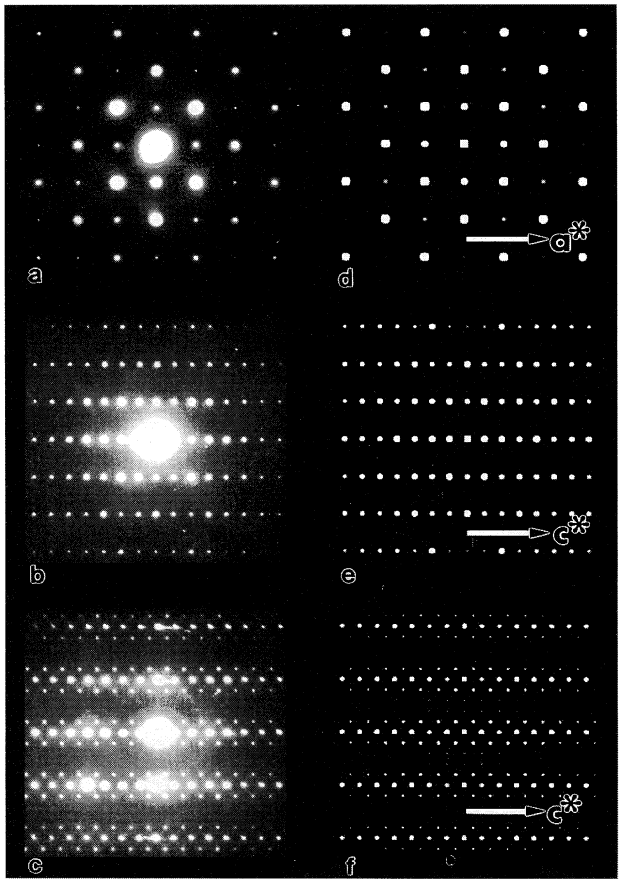

FIG. 5. Experimental electron diffraction patterns for the ⟨001⟩, ⟨100⟩, and ⟨110⟩ zone axes (a)–(c). Corresponding multislice simulations of the model in Fig. 6. Reflections due to the modulation are evident in the ⟨110⟩ zone axis (c) and (f) and are forbidden in the ⟨001⟩ and ⟨100⟩ (a), (b), (d), (e).

diffraction patterns were indexed based on the $HgBa_2CuO_{4+\delta}$ tetragonal unit cell. Sharp modulated reflections exist along $\mathbf{g}_{1/5\ 1/5\ 1/2}$ and $\mathbf{g}_{1/5\ -1/5\ 1/2}$ for all of the ⟨110⟩ patterns observed. The modulation was only found close to $\mathbf{g}_{1/5\ 1/5\ 1/2}$ or $\mathbf{g}_{1/5\ -1/5\ 1/2}$ and was also observed in the ⟨301⟩, ⟨112⟩, and ⟨111⟩ zone axes, but not on the ⟨100⟩ and ⟨001⟩ zone axes. The modulation is actually incommensurate with the reflections lying along $\mathbf{g}_{1/4.9\ 1/4.9\ 1/2}$; for simplicity, $\mathbf{g}_{1/5\ 1/5\ 1/2}$ will be used to approximate it. The presence of reflections along both $\mathbf{g}_{1/5\ 1/5\ 1/2}$ and $\mathbf{g}_{1/5\ -1/5\ 1/2}$, combined with the lack of a twin structure in ⟨110⟩ HREM images, requires the modulation to be in both directions. The modulation was identical under 100 and 300 kV electron imaging conditions, thus ruling out electron radiation damage.

A chemical ordering, based on a Cr content near 50%, was assumed in modeling the modulation. A $5a\times5a\times2c$ supercell was used to approximate the incommensurate modulation with a cosine-squared wave to model the Cr occupancy, with

$$\alpha\{\cos^2[\pi(x+y)]+\cos^2[\pi(x-y)]\}, \qquad (1)$$

defining the Cr occupancy in the first layer, and

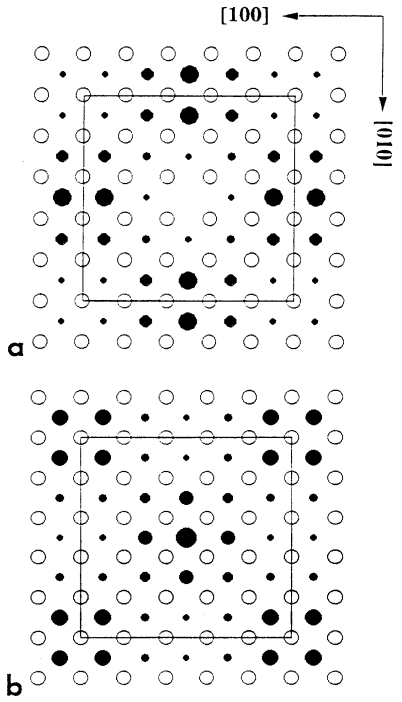

FIG. 6. Average occupancy of Cr atoms at Hg sites for two alternating Hg-O planes along the ⟨001⟩ axis. The occupancies in (a) and (b) are determined by Eqs. (1) and (2), respectively. Large open circles represent O atoms; solid circles of varying size represent Cr atoms. The sizes of the solid circles are proportional to the Cr fractional occupancies. The Hg occupancy is one minus the Cr occupancy.

$$1-\alpha\{\cos^2[\pi(x+y)]+\cos^2[\pi(x-y)]\}, \qquad (2)$$

defining the Cr occupancy in the second layer along the c axis, where x and y are along [100] and [010], respectively, and $\alpha=1$ for 50% Cr concentration. Because the ⟨001⟩ zone axis diffraction pattern does not show a modulation, the Cr and Hg composition must be homogeneous over the ⟨001⟩ projection. A cosine-squared wave is justified by the rapid damping of the higher-order modulated reflections in the diffraction patterns, e.g., Fig. 5(c). The Cr and Hg compositions for the two different layers are illustrated in Figs. 6(a) and 6(b), where the Hg occupancy is one minus the Cr occupancy on any given site. While the neutron data provide detail regarding the oxygen ordering, no modeling of oxygen site occupancies was attempted as the small electron-scattering factor of oxygen makes it difficult to detect. The displacement of the Cr atoms, deduced from the neutron-diffraction data, was also not modeled; instead, a random Cr displacement in ⟨100⟩ directions was approximated by a relatively large Debye-Waller term. Simulated diffraction patterns are shown in Figs. 5(d)–5(f) for each of the experimental zone axes presented in Figs. 5(a)–5(c), a good match was obtained for each.

Because there is little phase information in a diffraction pattern, any model constructed from diffraction patterns must be verified with HREM. Figure 7 shows a ⟨110⟩ HREM image with a multislice simulation based on the model in Fig. 6. The simulation provides a good visual fit with the experi-

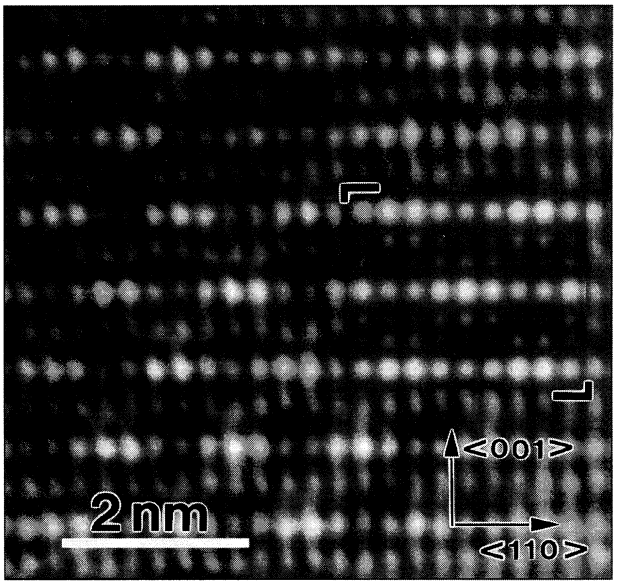

FIG. 7. Multislice image simulation of the model presented in Fig. 6 pasted into an experimental HREM image. The mean level of the simulation is the same as the local area into which it is pasted. Therefore, contrast variations may be directly compared. The modulation is evidenced by the broad fringes on the (225) and ($2\bar{2}5$) planes. The parameters used in the simulation are spherical aberration=0.9 mm, defocus=−150 nm, and thickness=8.1 nm.

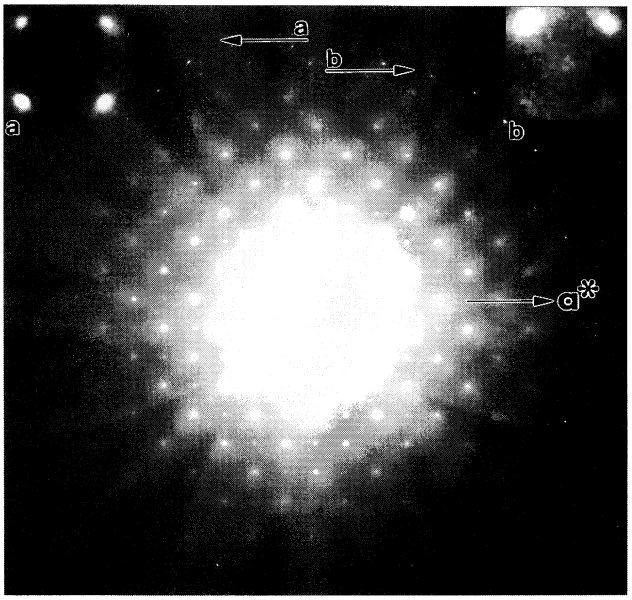

FIG. 8. A much longer exposure of the ⟨001⟩ pattern in Fig. 5(a) shows diffuse intensity and the first-order Laue zone. Chemical disorder is indicated by the presence of diffuse intensity at the forbidden Bragg locations for the modulation in the zero-order Laue zone [see inset (a)]. The Bragg reflections for the modulation are allowed in the first-order Laue zone and are easily seen as sharp spots [inset (b)].

mental image. It should be noted that the HREM simulation matches the experimental images on the large scale just as well as on the small scale. A small part was cut (about a supercell size which should present the whole structure) from a large picture of the simulated image to paste directly into the experimental image so that a more quantitative comparison could be made; i.e., the experimental mean level and the range of the intensity match the simulation as well. Such a fit should generally be considered insufficient without strong supporting data, e.g., the electron- and neutron-diffraction analyses. Simpler structures may be quantitatively refined to obtain the atomic positions;[17] however, the modulation presented here is too large and complicated for this method. The modulation is evident by the broad fringes in the (225) and ($2\bar{2}5$) planes. HREM of the ⟨100⟩ and ⟨001⟩ axes show the basic undoped structure as a result of the homogenous Cr concentration along these projections.

Evidence for chemical disorder can be seen in the c-axis diffraction pattern, shown in Fig. 8. The modulated reflections are forbidden in the zero-order Laue zone of the ⟨001⟩ zone axis: however, weak diffuse reflections are present at the Bragg locations for the modulation. The modulation has allowed Bragg reflections in the first-order Laue zone (FOLZ) and strong sharp reflections are evident. Our calculations show the FOLZ to be 17.5 $Å^{-1}$ along c^*, which clearly shows the doubling of the c axis. Several other zone axes, e.g., ⟨100⟩, in which the modulated reflections are forbidden also show diffuse intensity resulting from the chemical disorder.

Quantitative x-ray microanalysis in an analytical electron microscope (Hitachi HF-2000) was utilized in conjunction with standards for composition determination. Sensitivity factors (k factors) were obtained from $SrHgO_2$, $SrCuO_2$, and $SrCrO_4$ compounds. The overall cation composition is indicated in Table III. These measurements indicate a Cr concentration of 0.38(3) atoms per formula unit. This is consistent with the observation of $SrCuO_2$ and $SrHgO_2$ as minor impurity phases, suggesting a Cr concentration higher than the starting composition (0.3). Site occupancies obtained from the Rietveld refinement of neutron-diffraction data (Table I) can also be used to estimate the Cr content, but these can be subject to systematic errors when nonharmonic static displacements are present in the structure [as is certainly true for the Hg and O(2) atoms]. The average of Cr, O(2)′, and O(3) occupancies from the refinement suggests a Cr content of about 0.42, in reasonable agreement with the x-ray microanalysis. We conclude that the Cr content is near 0.4. Unsuccessful attempts to form other compositions with different Cr concentrations suggest that Cr may not form a continuous solid solution in this compound.

Electron-energy-loss spectroscopy (EELS) was employed to determine the valence state (and coordination) for Cr ions

TABLE III. Quantitative x-ray microanalysis. The numbers are normalized to two strontium atoms per unit cell.

Element	Nominal composition	Chemical analysis
Hg	0.7	0.73(3)
Cr	0.3	0.38(3)
Sr	2	2
Cu	1	1.04(8)

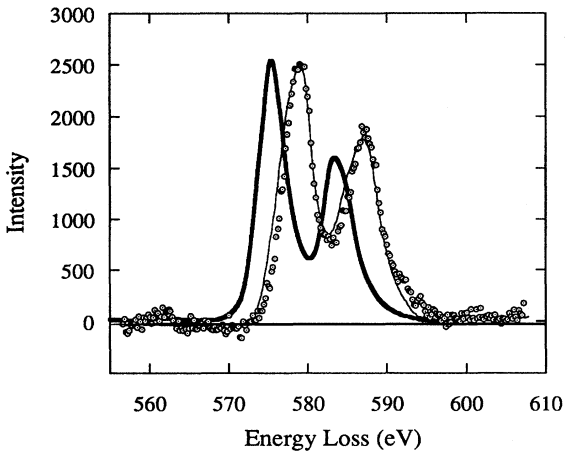

FIG. 9. Cr_{L23} EELS spectra from $Hg_{1-x}Cr_xSr_2CuO_{4+\delta}$ (data) are compared with those from CrO_3 and Cr_2O_3 (narrow and bold solid lines, respectively). The absorption energy onset, near-edge structure, and $L2/L3$ ratios provide a consistent picture that Cr is in a 6+ valence state (as for Cr^{6+} in CrO_3).

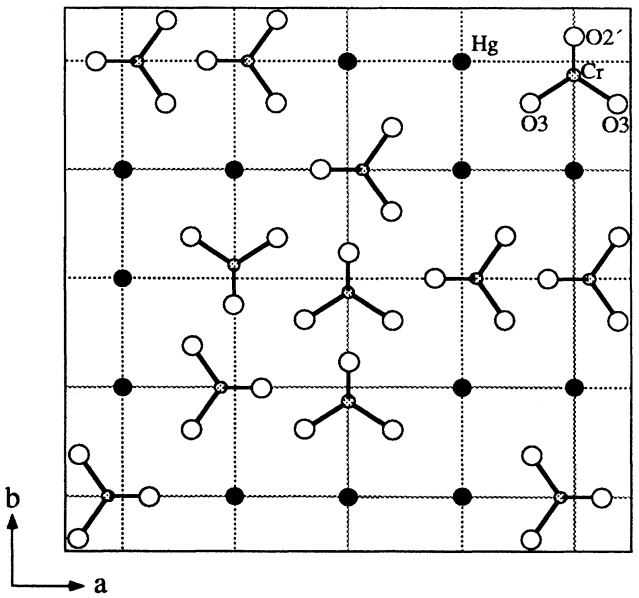

FIG. 10. Representation of one layer of the a-b plane of $Hg_{1-x}Cr_xSr_2CuO_{4+\delta}$ showing a possible arrangement of CrO_4 units on the available sites to form a cluster that agrees with the probability illustrated in Fig. 6(b). Frustration of the orientation of CrO_4 units requires disorder in the cluster and limits cluster size.

in the structure.[18] Cr_{L23} absorption edge fine structure for $Hg_{1-x}Cr_xSr_2CuO_{4+\delta}$ was compared with that for CrO_3 and Cr_2O_3, as shown in Fig. 9. It is notable that the absorption energy onset for the Cr_{L23} edge in $Hg_{1-x}Cr_xSr_2CuO_{4+\delta}$ is significantly higher [by 3.4(±0.4) eV] than that from Cr_2O_3, indicating a higher oxidation state for chromium. The absorption energy onset, the energy loss near edge structure, and the $L2/L3$ intensity ratio are consistent with a Cr valence of 6+, as was also concluded from its tetrahedral coordination in the structure and from the short Cr-O bond lengths.

For simple chromate compounds, a tetrahedral environment is typically found for both Cr^{5+} and Cr^{6+} [$r(Cr^{5+})$ is slightly larger than $r(Cr^{6+})$] in which Cr-O bond lengths are approximately 1.66 Å (for example, ammonium salts). In more complicated structures where a network of Cr tetrahedra exists, Cr-O bond lengths of 1.75 Å are found.[19] These values are in good agreement with those found in $Hg_{1-x}Cr_xSr_2CuO_{4+\delta}$; two Cr-O bond lengths are 1.656 and 1.732 Å. Also, the tetrahedral angles of 107.7°, 114°, and 112° are in reasonable agreement with structural data of other chromates. For example, in CrO_2Cl_2 the tetrahedral angles are 105°, 113°, and 109.5°.[19] The similarity between the crystal chemistry of Cr^{5+} and Cr^{6+} does suggest that in $Hg_{1-x}Cr_xSr_2CuO_{4+\delta}$, Cr may assume either charge state or both. However, as shown above, the results from EELS conclusively demonstrate that Cr is in the 6+ state.

DISCUSSION AND CONCLUSIONS

A simplified picture of the supercell structure is that Cr-rich regions of dimensions $2.5a \times 2.5a \times c$ (9.6×9.6×8.7 Å^3) alternate in all three dimensions with Hg-rich regions (which have a nearly normal $HgBa_2CuO_{4+\delta}$ structure except for the shortened apical bond length). Perpendicular to the ⟨001⟩ axis, distorted CuO_2 planes mark the boundaries between these regions. Because the apical Cu-O bond in the direction of Cr is elongated to 3.13 Å while that in the direction of Hg is shortened to 2.25 Å, the conduction plane is best viewed as consisting of CuO_5 pyramids (pointing towards Hg) rather than CuO_6 octahedra. These pyramids point up or down in accordance with the supercell.

The local structure, learned from neutron powder diffraction, provides important insight concerning why the superstructure forms. The cell doubling along the c axis occurs because of the tendency for Hg and Cr to alternate along this direction. A local structure in which Cr is present both above and below the same Cu atom is energetically unfavorable because it requires the Cu atom to be in square planar coordination (nominally Cu^{3+}) rather than pyramidal or octahedral coordination. The size of Cr clusters in the a-b plane is limited by frustration effects involving the O(3) oxygen atoms, as illustrated in Fig. 10. Each Cr atom is bonded to two O(3) atoms in the plane. This places constraints on the orientation of CrO_4 units as the size of the cluster grows. At a cluster size of two to three fundamental unit cell dimensions, it is no longer possible to add additional CrO_4 units. Figure 10 shows only one layer, but the problem becomes even more constrained when the next layer along the c axis is considered, where, for 50% Cr content, CrO_4 units are located above Hg atoms in the first layer. From these considerations we can see that frustration in the orientation of CrO_4 units limits the cluster size to about 2.5 cell dimensions, in agreement with the supercell observed by electron diffraction. Additionally, we can conclude that the solubility for Cr is likely to be less than 50%. We also see that considerable disorder, resulting from different ways to orient individual CrO_4 units, will be present in the supercell.

From the structural features determined in this study, it is not clear why this solid-solution compound should exhibit

enhanced flux pinning. The Cr- and Hg-rich regions are smaller than typical magnetic vortex dimensions and are regularly arranged in the crystal. Thus the average superstructure does not define any preferred location for a vortex. If extended defect formation contributes to flux pinning, it must involve defects in the superstructure. Since the supercell is necessarily disordered, extended defect formation is likely. However, such defects are beyond the length scale investigated in this work. We can speculate on two possibilities. For Cr contents near, but less than, 50%, the Hg-rich regions may form extended defects. A likely arrangement would involve columns of Hg-containing cells extending along the c axis. From the point of view of the CuO_2 planes, these would be columns of CuO_6 octahedra embedded in the supercell, which consists of CuO_5 pyramids. Such extended defects could act somewhat like columnar defects produced by radiation damage, which are known to be effective flux pinners.[6–11] A second possible defect, which would be most likely in dilute Cr concentrations, would involve diagonal chains of Cr in ⟨101⟩ directions (based on the fundamental cell). Clearly, if such defects play an important role in flux pinning, the effects would depend on Cr concentration. Experiments as a function of concentration have not been done and may prove to be difficult based on the limited solubility range suggested by our work.

The ability to enhance flux pinning by chemical substitution could have important consequences for the application of copper-oxide superconductors. The results of this study suggest that structural modifications in which clustering and extended defect ordering occur should be investigated. A troublesome side effect is that such defects can significantly distort the CuO_2 plane and may substantially lower T_c. The highest T_c's are thought to be achieved for flat CuO_2 planes and long Cu-O apical bonds, as are present in the $HgBa_2Ca_{n-1}Cu_nO_{2n+2+\delta}$ compounds.[14,20,21] The effect of distortions of the CuO_2 plane have been studied in $La_{2-x}M_xCuO_4$ (M=Sr, etc.) compounds, where T_c decreases systematically as the tilt angle of the CuO_6 octahedra increases.[22–24] One would like to enhance flux pinning as much as possible while minimizing the decrease in T_c caused by the chemical substitution. Thus, in future work, it will be important to investigate the structural effects of different chemical substitutions and the effects of varying the defect concentration, especially in the dilute limit.

ACKNOWLEDGMENTS

We wish to acknowledge useful discussions with G. W. Crabtree, U. Welp, K. E. Gray, J. F. Mitchell, and K. R. Poeppelmeier. This work was supported by the U.S. Department of Energy, Division of Basic Energy Science—Materials Sciences, under Contract No. W-31-109-ENG-38 (J.D.J. and D.G.H.) and by the National Science Foundation, Office of Science and Technology Centers under Grant No. DMR 91-20000 (O.C., D.N.A., B.G.S., H.Z., L.D.M., Y.Y.W., V.P.D., B.D.).

[1] J. Shimoyama, S. Hahakura, R. Kobayashi, K. Kitazawa, K. Yamafuji, and K. Kishio, Physica C **235-240**, 2795 (1994).

[2] J. Shimoyama, K. Kishio, S. Hahakura, K. Kitazawa, K. Yamaura, Z. Hiroi, and M. Takano, in *Advances in Superconductivity VII*, Proceedings of the 7th International Symposium on Superconductivity (ISS'94), Kitakyushu, edited by K. Yamafuji and T. Morishita (Springer-Verlag, Tokyo, 1995).

[3] J. Shimoyama, S. Hahakura, K. Kitazawa, Y. Yamafuji, and K. Kishio, Physica C **224**, 1 (1994).

[4] K. E. Gray and D. H. Kim, Physica C **180**, 139 (1991).

[5] K. E. Gray, Appl. Supercond. **2**, 295 (1994).

[6] J. Schwartz and Shiming Wu, J. Appl. Phys. **73**, 1343 (1993).

[7] J. Schwartz *et al.*, IEEE Trans. Appl. Supercond. **AS-3**, 1652 (1993).

[8] W. Gerhauser, H.-W. Neumuller, W. Schmidt, G. Ries, G. Saemann-Ischenko, H. Gerstenberg, and F.-M. Sauerzopf, Physica C **185-189**, 2273 (1991).

[9] W. Kritscha, F. M. Sauerzopf, H. W. Weber, G. W. Crabtree, Y. C. Cheng, and P. Z. Jiang, Europhys. Lett. **12**, 179 (1990).

[10] H. W. Weber, Supercond. Sci. Technol. **5**, S19 (1992).

[11] B. M. Vlcek, M. C. Frischherz, S. Fleshler, U. Welp, J. Z. Liu, J. Downey, K. G. Vandervoort, G. W. Crabtree, M. A. Kirk, J. Giapintzakis, and J. Farmer, Phys. Rev. B **46**, 6441 (1992).

[12] J. D. Jorgensen, J. Faber, Jr., J. M. Carpenter, R. K. Crawford, J. R. Haumann, R. L. Hitterman, R. Kleb, G. E. Ostrowski, F. J. Rotella, and T. G. Worlton, J. Appl. Crystallogr. **22**, 321 (1989).

[13] A. C. Larson and R. B. Von Dreele, General Structure Analysis System, University of California, Berkeley, 1985–1990.

[14] J. L. Wagner, P. G. Radaelli, D. G. Hinks, J. D. Jorgensen, J. F. Mitchell, B. Dabrowski, G. S. Knapp, and M. A. Beno, Physica C **210**, 447 (1993).

[15] J. D. Jorgensen, B. W. Veal, A. P. Paulikas, L. J. Nowicki, G. W. Crabtree, H. Claus, and W. K. Kwok, Phys. Rev. B **41**, 1863 (1990).

[16] Y. Shimakawa, J. D. Jorgensen, D. G. Hinks, H. Shaked, R. L. Hitterman, F. Izumi, T. Kawashima, E. Takayama-Muromachi, and T. Kamiyama, Phys. Rev. B **50**, 16 008 (1994).

[17] H. Zhang, L. D. Marks, Y. Y. Wang, H. Zhang, V. P. Dravid, P. Han, and D. A. Payne, Ultramicroscopy **57**, 103 (1995).

[18] J. J. Paterson and O. L. Krivanek, Ultramicroscopy **32**, 319 (1990).

[19] A. F. Wells, *Structural Inorganic Chemistry*, 4th ed. (Clarendon, Oxford, 1975).

[20] P. G. Radaelli, J. L. Wagner, B. A. Hunter, M. A. Beno, G. S. Knapp, J. D. Jorgensen, and D. G. Hinks, Physica C **216**, 29 (1993).

[21] J. L. Wagner, B. A. Hunter, D. G. Hinks, and J. D. Jorgensen, Phys. Rev. B **51**, 15 407 (1995).

[22] B. Buchner, M. Breuer, A. Freimuth, and A. P. Kampf, Phys. Rev. Lett. **73**, 1841 (1994).

[23] B. Dabrowski, Z. Wang, K. Rogacki, J. D. Jorgensen, R. L. Hitterman, J. L. Wagner, B. A. Hunter, and D. G. Hinks, Physica C **217**, 455 (1993).

[24] H. Takahashi, H. Shaked, B. A. Hunter, P. G. Radaelli, R. L. Hitterman, D. G. Hinks, and J. D. Jorgensen, Phys. Rev. B **50**, 3221 (1994).

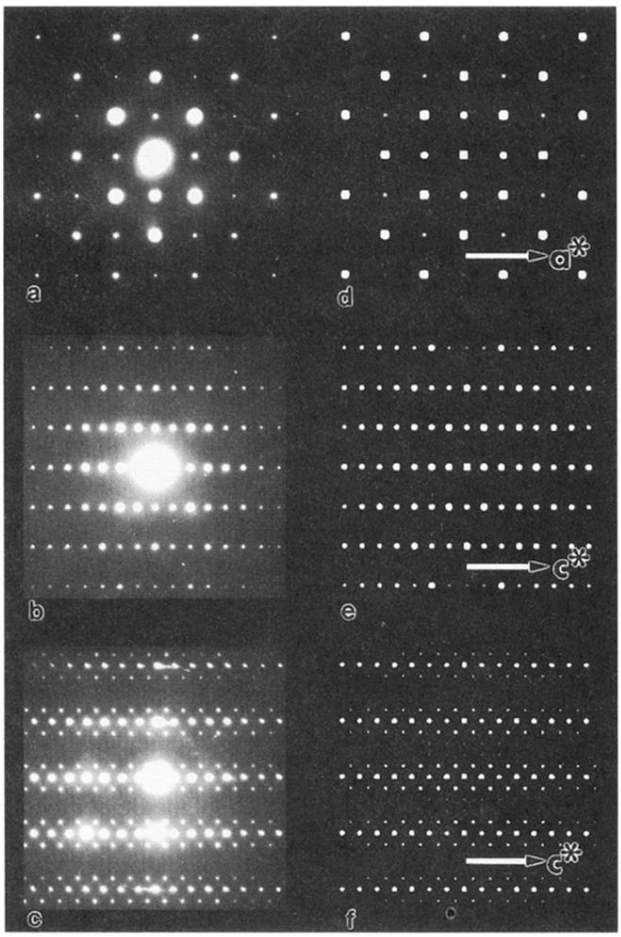

FIG. 5. Experimental electron diffraction patterns for the ⟨001⟩, ⟨100⟩, and ⟨110⟩ zone axes (a)–(c). Corresponding multislice simulations of the model in Fig. 6. Reflections due to the modulation are evident in the ⟨110⟩ zone axis (c) and (f) and are forbidden in the ⟨001⟩ and ⟨100⟩ (a), (b), (d), (e).

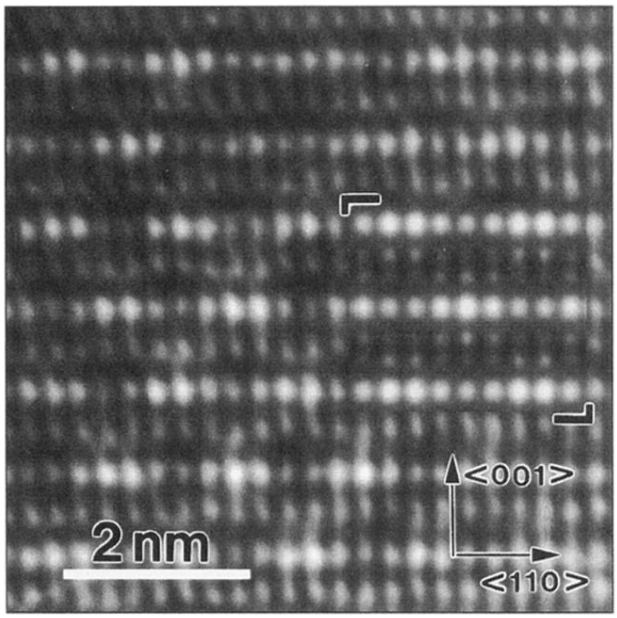

FIG. 7. Multislice image simulation of the model presented in Fig. 6 pasted into an experimental HREM image. The mean level of the simulation is the same as the local area into which it is pasted. Therefore, contrast variations may be directly compared. The modulation is evidenced by the broad fringes on the (225) and ($2\bar{2}5$) planes. The parameters used in the simulation are spherical aberration=0.9 mm, defocus=−150 nm, and thickness=8.1 nm.

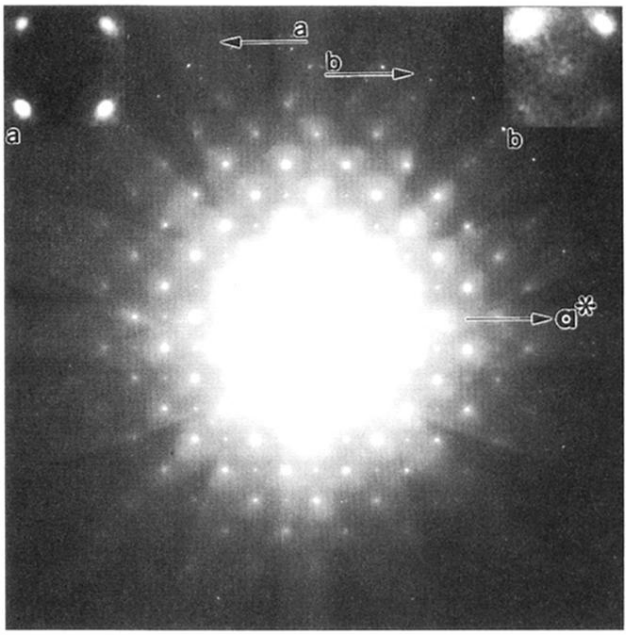

FIG. 8. A much longer exposure of the ⟨001⟩ pattern in Fig. 5(a) shows diffuse intensity and the first-order Laue zone. Chemical disorder is indicated by the presence of diffuse intensity at the forbidden Bragg locations for the modulation in the zero-order Laue zone [see inset (a)]. The Bragg reflections for the modulation are allowed in the first-order Laue zone and are easily seen as sharp spots [inset (b)].